3D Bioprinting of a stem cell-laden, multi-material tubular composite: an approach for spinal cord repair

Omar A Hamid[ab*], Hoda M Eltaher[bc], Virginie Sottile[de*] and Jing Yang[b]

[a]Pharmaceutics Division, College of Pharmacy, University of Mosul, 41002 Mosul, Iraq. Email: omar.hamid@uomosul.edu.iq

[b]Regenerative Medicine and Cellular Therapies Division, Faculty of Science, University of Nottingham, University Park, Nottingham NG7 2RD, UK. (Affiliation at the time of this work).

[c]Department of pharmaceutics, Faculty of Pharmacy, Alexandria University, Egypt, 21521. Email: Hoda.amin@alexpharmacy.edu.eg

[d]School of Medicine, University of Nottingham, University Park, Nottingham NG7 2RD, UK.

[e]Department of Molecular Medicine, The University of Pavia, 27100 Pavia, Italy. Email: virginie.sottile@unipv.it.

Jing Yang email address: Jing.yang@nottingham.ac.uk

*Corresponding authors

Abstract

Development of a biomimetic tubular scaffold capable of recreating developmental neurogenesis using pluripotent stem cells offers a novel strategy for the repair of spinal cord tissues. Recent advances in 3D printing technology have facilitated biofabrication of complex biomimetic environments by precisely controlling the 3D arrangement of various acellular and cellular components (biomaterials, cells and growth factors). Here, we present a 3D printing method to fabricate a complex, patterned and embryoid body (EB)-laden tubular scaffold composed of polycaprolactone (PCL) and hydrogel (alginate or gelatine methacrylate (GelMA)). Our results revealed 3D printing of a strong, macro-porous PCL/hydrogel tubular scaffold with a high capacity to control the porosity of the PCL scaffold, wherein the maximum porosity in the PCL wall was 15%. The method was equally employed to create spatiotemporal protein concentration within the scaffold, demonstrating its ability to generate linear and opposite gradients of model molecules (fluorescein isothiocyanate-conjugated bovine serum albumin (FITC-BSA) and rhodamine). 3D bioprinting of EBs-laden GelMA was introduced as a novel 3D printing strategy to incorporate EBs in a hydrogel matrix. Cell viability and proliferation were measured post-printing. Following the bioprinting of EBs-laden 5% GelMA hydrogel, neural differentiation of EBs was induced using 1 μM retinoic acid (RA). The differentiated EBs contained βIII-tubulin positive neurons displaying axonal extensions and cells migration. Finally, 3D bioprinting of EBs-laden PCL/GelMA tubular scaffold successfully supported EBs neural differentiation and patterning in response to co-printing with 1 μM RA. 3D printing of a complex heterogeneous tubular scaffold that can encapsulate EBs, spatially controlled protein concentration and promote neuronal patterning will help in developing more biomimetic scaffolds capable of replicating the neural patterning which occurs during neural tube development.

Keywords: 3D printing, hydrogels, polycaprolactone, gradient, embryoid body (EB), neural differentiation and nerve regeneration.

1 Introduction

Central nervous system (CNS) disorders, caused by injuries or neurodegenerative diseases, are a leading cause of disabilities and death [1, 2]. Unfortunately, all available medicines are for relieving the symptoms or delaying the progression of the diseases. The mammalian CNS is characterised by its very limited self-repair ability [3, 4], therefore there is a critical need for novel regenerative strategies that promote tissue repair [1]. Over the last decades, different regenerative strategies have been suggested for promoting brain or spinal cord repair, including direct cell transplantation, direct growth factor injections and tissue engineering strategies based on the combination of biomaterial, stem cells and growth factors [2, 5]. Tissue engineering strategies have shown promising outcomes in promoting tissue repair when compared to direct cell transplantation or growth factor injection [1, 6]. However, there are still substantial challenges in creating a functional scaffold to serve as a nerve conduit or tissue graft to repair the damaged spinal cord. Among these challenges is the development of a tubular structure having the key design parameters of spinal cord scaffold such as mechanical properties, porosity and patterning of the physicochemical cues that can control stem cell differentiation [7]. Addressing these challenges would be key for improving success in CNS repair [2, 8, 9]

During embryogenesis, CNS development including the spinal cord is tightly controlled by gradients of morphogens which direct neuroprogenitor differentiation into different mature neurons in a concentration-dependent manner [10, 11]. For example, patterning along the rostral-caudal axis results from opposite gradients of retinoic acid (RA) and fibroblast growth factor (FGF)[12]. Also, neural cell migration and axonal growth cone guidance are regulated by the concentration gradient of signalling molecules [13, 14]. Accordingly, fabrication of a bioinspired tubular scaffold with a spatially controlled concentration of a soluble biochemical agent and the encapsulation of neural progenitor cells could help in developing a spatially-patterned spinal cord graft [15].

3D printing has emerged in the field of tissue engineering as a flexible and programmable biofabrication technology to address the structural challenges of developing biomimetic tissue-like constructs. It has the capacity for precise layer-by-layer deposition of multi-materials based on a pre-designed pattern. This provides a high degree of spatial control over physical and chemical cues in the scaffolds such as porosity, mechanical properties and bioactive molecules concentrations or gradients [16]. Furthermore 3D printing facilitates the production of patient-customised tubular scaffold for repairing damaged nerve [15]. Several techniques such as hydrogel casting or microfluidics have been used to create a patterned differentiation of embryoid bodies (EBs), which equivalent to the neural progenitor cells during embryogenesis, recapitulating some aspects of the natural development process. A hybrid micro-hydrogel platform (GelMA/PEG) was developed to create an anisotropic stem cell niche for patterned differentiation of

EBs [17]. A microfluidic device was also used to generate spatially patterned EBs [18]. Despite the great progress in fabrication techniques, simple hydrogel casting has a limited capacity to generate spatially and/or temporally patterned microenvironments [16]. For example, EBs are usually surrounded by homogeneously dispersed signalling molecules, lacking spatial and/or temporal control of these molecules within the 3D matrix [19]. Moreover, this traditional approach has a limited capacity to precisely control the internal and external architecture (such as porosity) and mechanical properties [20, 21]. Microfluidic devices have overcome some of these challenges by creating 3D spatiotemporal patterns of growth factors, however, they have limited potential for clinical applications [22]. These challenges have propelled the employment of 3D printing to fabricate a complex biomimetic model [19, 23, 24]. This current study aims to develop a 3D printing method to fabricate a hydrogel-based tubular scaffold capable of directing the neural differentiation of ESCs. To achieve this aim, 3D printing was used to produce a macro-porous hydrogel tubular scaffold with a protein gradient pattern and seed EBs. Finally, the scaffold was used to test neural differentiation and patterning as a proof of concept. The approaches used in this study will help develop more complex models that can more faithfully recapitulate neural tube morphogenesis.

2 Materials and methods

All chemicals were purchased from Sigma-Aldrich, UK unless otherwise stated.

2.1 3D Printing of PCL-alginate scaffolds

Stock alginate solution (3% w/v) in Ca-free Dulbecco's Modified Eagle's Medium (DMEM) media (Gibco Life Technologies, Paisley, UK) was prepared using a roller mixer (Stuart, Biotechnology Medical Service, France) (50 rpm) overnight. The stock alginate was then diluted at 2:1 ratio with either Ca-free DMEM or FITC-BSA (6 mg/mL) depending on the experiment. The resultant alginate solutions were partially crosslinked with 30 mM $CaCl_2$ solution at alginate: $CaCl_2$ ratio 2:1 to achieve final alginate and $CaCl_2$ concentrations of 1.5 % (w/v) and 10 mM, respectively. FITC-BSA final concentration was 1 mg/mL. Mixing of alginate and $CaCl_2$ solutions was performed using two luer-lock syringes (Becton Dickinson, USA), one for the alginate and the other one for $CaCl_2$, connected by a female-female luer-lock connector and the mixture was mixed repeatedly between the two syringes (40 times, at mixing rate 1Hz).

The scaffolds were printed using an extrusion-based multi-head 3D printer (RegenHU, 3D Discoveries, Switzerland). All the designs were performed using computer-aided manufacturing software (BioCAD, RegenHU, Switzerland) that contains information for layer by layer built up of 3D constructs, includes printing head, line space and offset, layer thickness and building height. This information was then translated into a numerical code (G code) and exported into printer's software. The PCL-alginate tubular scaffold was designed and printed in two steps as shown in **figure-1-a**. In step 1, a hollow PCL tubular frame was printed using the thermoplastic polymer print head. PCL granules (45 kDa) were allowed to melt into the thermoplastic polymer cartridge at 73°C. PCL was extruded through a stainless straight needle (6.5 mm × 0.33 mm) (length × internal diameter). The print head speed was 20 mm/s and layer thickness was 0.12 mm. The hollow PCL frame consisted of two concentric cylinders (inner and outer) printed simultaneously inside each other. The cylinders are separated by a 2 mm gap and connected at the tube base (**figure 1-a**).

To maintain oxygen and nutrient diffusion into the hydrogel-encapsulated cells, the inner PCL cylinder was made macro-porous. The pores in the PCL frame were generated by printing two groups of repeated-circular layers, continuous and non-continuous circular layers, in an alternative manner (**figure 1-c**). Each non-continuous circular layer was composed of 4 incomplete opposite arcs separated by 4 opposite gaps (4 pores). The subsequent non-continuous layer group had also 4 pores but with a 45° degree misalignment (**figure 1-c and figure 1-d**). As a result, 8 longitudinally-aligned columns of pores were produced along with the PCL cylinder.

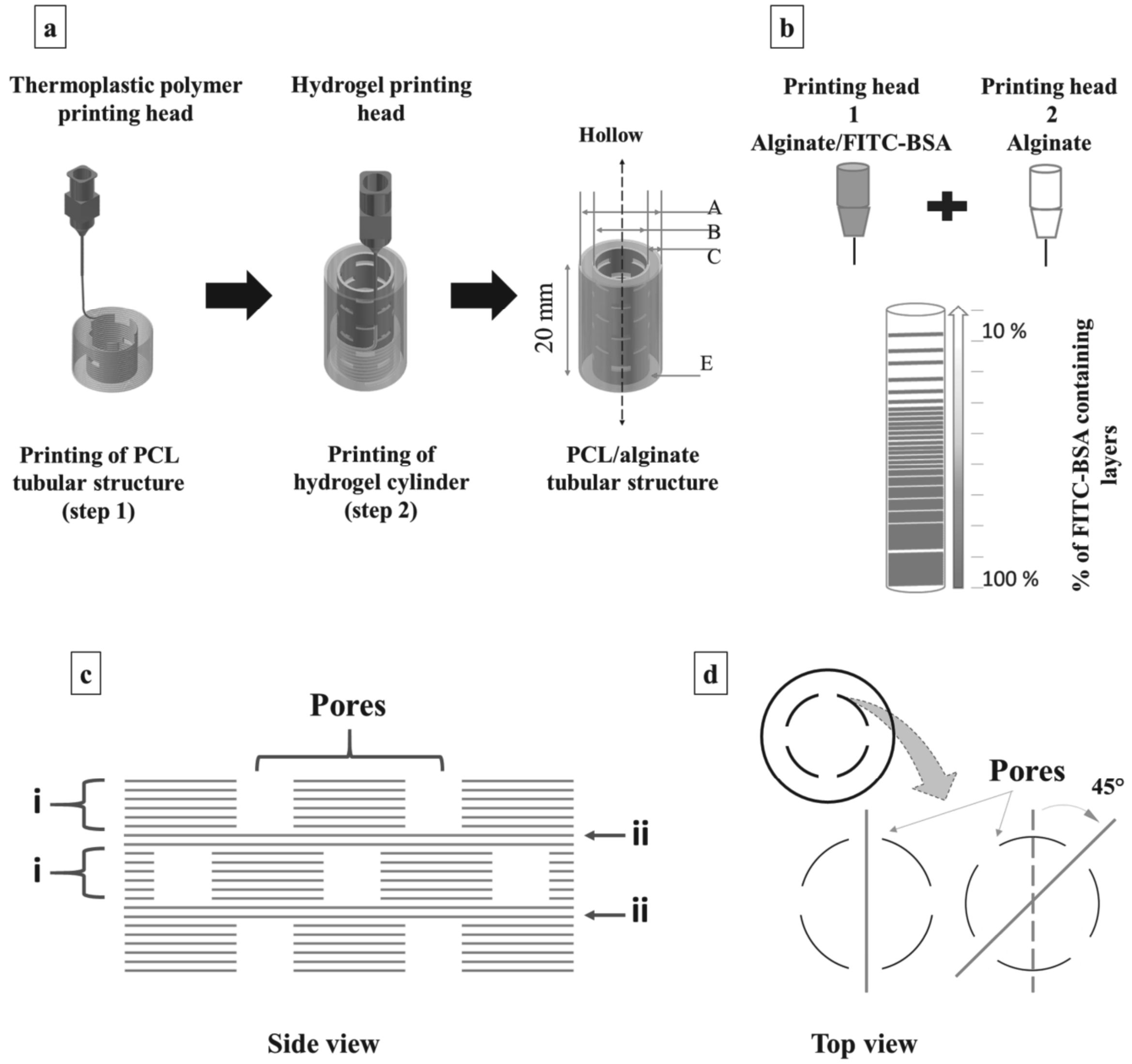

Figure 1 Schematic presentation of the 3D printing approach for making the PCL-alginate scaffold. In step 1, a porous PCL tubular structure was printed; dimensions of the structure (mm): A=12, B=10, C=2. In step 2, (**a**) alginate hydrogel cylinder was printed in the space between the inner and outer PCL cylinders using a long straight needle (G22 or G25, 2.54 cm length), (**b**) Method for making a FITC-BSA concentration gradient. Schematic showing 3D printing of the porous PCL cylinder; (**c**) Side view of the pores fabricated by alternate printing of two groups of layers: (**i**) non-continuous (blue) and (**ii**) continuous (red). (**d**) Top schematic view of the porous PCL cylinder, showing the position of the pores in the non-continuous layers.

In the second step, plain or FITC-BSA mixed partially cross-linked alginate hydrogels (1.5%) were printed inside the space between the two PCL cylinders. Circular layers were printed inside the PCL structure using a long straight needle (G25 or G22 and 1 inch long). To ensure effective filling of the gap between the PCL cylinders and to maintain a constant space between the needle tip and the printed alginate surface, the hydrogel flow rate was optimised to 0.045g/min/0.1mm layer thickness. The layer thickness was set to 0.1 or 0.2 mm for structures of 10 mm or 20 mm height, respectively. The scaffolds were then immersed in 100 mM $CaCl_2$ for 20 min for crosslinking. For printing of EB-laden scaffolds, EB-laden 5% GelMA was printed inside the PCL scaffolds using a G20 needle and the GelMA was cured under UV light for 1 min.

2.2 3D Printing of FITC-BSA-gradient pattern

The gradient pattern of the FITC-BSA was printed using two partially crosslinked alginate hydrogel (1.5%) dispensers, one loaded with 1 mg/mL FITC-BSA and the other with plain hydrogel. The gradient was designed as a 10-step pattern, each of which is comprised of 10 layers with a 10 % reduction in the number of layers that contain FITC-BSA between successive steps to produce a linear reduction in the amount of the delivered FITC-BSA as a function of scaffold distance (**figure 1-b**).

For validation of the gradient pattern, 10 mm long FITC-BSA gradient-patterned scaffolds were sectioned using a cryostat machine (Leica CM1100, Germany**)** and quantified for FITC-BSA retained in each respective section[25]. Briefly, the scaffolds were fixed in optimum cutting temperature (OCT) medium (Sakura Finetek USA, Inc) for 30 min at -80 ºC and sliced into 0.5 mm thick stacks (fifty 10 µm-slices) perpendicular to the direction of the gradient. Stacks were collected sequentially and dissolved in 400 µL of 150 mM sodium citrate. The de-crosslinked hydrogel was then centrifuged at 5000 rpm for 5 min to spin down any remaining PCL fibers and measured, in triplicates, for fluorescence intensity using TECAN infinite 200PRO multiple mode reader against a calibration curve of FITC-BSA. Calibration curve data was constructed using consistent single FITC-BSA concentrations in 0.5 mm thick slices of 3D printed PCL-alginate.

2.3 mESCs culture and neural differentiation

The feeder-free mESC cell line CGR8 (Sigma -Aldrich, UK) was cultured on gelatine (0.1%) -coated T-25 flasks. The cells were kept in an undifferentiated state in mESC culture medium (**supplementary information**). Differentiation of mESCs into spinal cord motor neurons was promoted following the protocol described by Wichterle and Peljto (2008) [26]. Briefly, mESCs were trypsinised and suspended in N2B27 (**supplementary information**) at a cell density of 200, 000 cell / mL for two days to form EBs (mass suspension method). After two days, the EBs were collected into 50-mL conical bottom plastic centrifuge tubes through a 100-µm cell strainer (Coring Incorporated, USA) to select EBs smaller than 100 µm for neural differentiation. EBs were then re-seeded into non-treated tissue culture 10 cm petri-dish and supplemented with fresh N2B27 medium supplemented with 1 µM RA. After 3 days (differentiation day 5), the medium was refreshed with RA-free N2B27 medium for 8 and 14 days based on the experiment.

2.4 Preparation of EB-laden gelatine methacrylate (GelMA) hydrogel

Lyophilised GelMA was synthesized by direct reaction of gelatine and methacrylate anhydride[27] and characterised using ^{1}HNMR (**figure S1**, **supplementary information**). 5% GelMA solution was prepared in warm Phosphate saline buffer (PBS) (60ºC) containing 0.5% photo-initiator (2-Hydroxy-4′-(2-hydroxyethoxy)-2-methylpropiophenone, 98%). The mixture was kept at 60ºC for 20 min to ensure that GelMA was completely dissolved in PBS. Thereafter, the warm GelMA was sterilised by filtration using a 0.2 µm filter and allowed to cool down before mixing with EBs. EBs were suspended in 5% GelMA (at density EBs produced from one 10 cm petri-dish / 1 mL of GelMA). The EBs-laden GelMA was uploaded into a 3D printer barrel and cooled down immediately at -15°C for 3-5 min to induce rapid physical crosslinking of GelMA and prevent EBs settling down. The barrel was then transferred to the 3D printer head which was equipped with a temperature adaptor (temperature set was 18°C). After printing of the GelMA hydrogel, all structures were exposed to UV light (using 365 nm UV lamp) for 1min to photo-crosslink the GelMA hydrogel.

2.5 3D printing of EBs in PCL-GelMA scaffold

For 3D printing of EBs in PCL-GelMA scaffold, a PCL scaffold (10 mm × 12 mm) (height × outer diameter) was first printed (as described in section 2.1) and then EBs-laden 5% GelMA was printed inside PCL using a straight G20 needle (600 µm × 0.5 inch) (diameter × length). Flow rate of GelMA, printing speed and layer thickness were kept constant as for the printing of PCL-alginate scaffolds. Thereafter, the whole scaffold was put in upright position under the UV lamp for 1 min to allow photo-crosslinking of GelMA through the opened top of the scaffold [28].

2.6 Cell viability and Proliferation

Cell viability was evaluated using the LIVE/DEAD® Viability/Cytotoxicity Kit for mammalian cells (Molecular Probes, USA). Following the manufacturer's protocol, 2 µM calcein AM / 4 µM EH-1 in PBS (working solution) was used to stain live cells (green) and dead cells (red). The structures were incubated with the working solution for 1.5 h at 37°C 5% CO_2. Thereafter, the live and dead cells are visualised using a confocal microscope (LEICA LSI-Z6A, UK). PrestoBlue® Cell proliferation assay (Invitrogen, USA) was used to evaluate the cell proliferation rate. The 3D structures were incubated with a working solution (10% PrestoBlue reagent in culture medium) for 4 h at 37°C 5% CO_2. 100 µL-aliquots were then collected for fluorescence intensity measurement using a TECAN infinite 200PRO multiple mode reader.

2.7 Immunocytochemistry (co-immunostaining)

EBs differentiated in 3D hydrogel matrices were stained following the general protocol of immunostaining with extended periods of incubations with reagents and antibodies and washing (the method is detailed in the **supplementary information**).

2.8 Statistical analysis

All the results were expressed as mean ± SD. Statistical analysis was performed using Graph pad prism 6 software. Data sets were tested for statistical significance using two-way ANOVA with Tukey's multiple comparisons test. Results were considered statistically significant if $P < 0.05$ and the significance levels were * $P < 0.05$, ** $P < 0.01$, *** $P < 0.001$ and **** $P < 0.0001$.

3 Results

3.1 3D printing of a tubular scaffold

A mechanically stable, macro-porous tubular scaffolds were printed using two different biomaterials; PCL and partially cross-linked alginate. The 3D reconstructed μCT image of the PCL scaffold shows a regular tubular structure composed of two concentric cylinders (**figure 2-a)**. The optical images revealed a hollow hybrid tubular scaffold composed of three concentric cylinders, two PCL cylinders (the outer and inner cylinders) and a middle hydrogel cylinder which was printed in the space between the PCL cylinders (**figure 2 b-d**).

To maintain oxygen and nutrient supply to cells encapsulated in the hydrogel cylinder, the inner PCL cylinder was printed as a macro-porous structure. The macro-pores were created in the cylinder surface by printing specific patterns of non-continuous and continuous PCL layers (**figure 1-c**). By controlling the number of layers per non-continuous or continuous layers, the overall porosity of the cylinder could be controlled. PCL cylinders, with nine different patterns, were printed (by varying the ratio of continuous and non-continuous rings) and thereafter characterised for porosity using image analysis. **Figure 2-e** shows bright field images of the porous PCL cylinders printed with different porosity patterns. The images revealed that pore density was inversely proportional to the number of layers in both continuous-layer and non-continuous-layer groups. However, the size of every single pore increased with the increase of the number of layers in the non-continuous layer group, indicating an increase in the overall PCL surface porosity as the number of layers in continuous-layers groups was reduced and the number of layers in the non-continuous-layers group was increased. To further confirm this finding, the overall porosity, expressed as a percentage of pores area / total area, was analysed. There was a significant increase in the porosity of the PCL cylinder with a concurrent increase in the number of non-continuous and a decrease in the number of continuous layers (**figure 2-f)**. The highest porosity (15.1 ± 1%) was found for non-continuous/continuous layers with a 6/2 ratio, and this ratio was selected for subsequent scaffold printing. These results demonstrated the capacity of a multi-head printer to generate hybrid PCL/hydrogel tubular scaffolds with precise control of the porosity of the PCL scaffold.

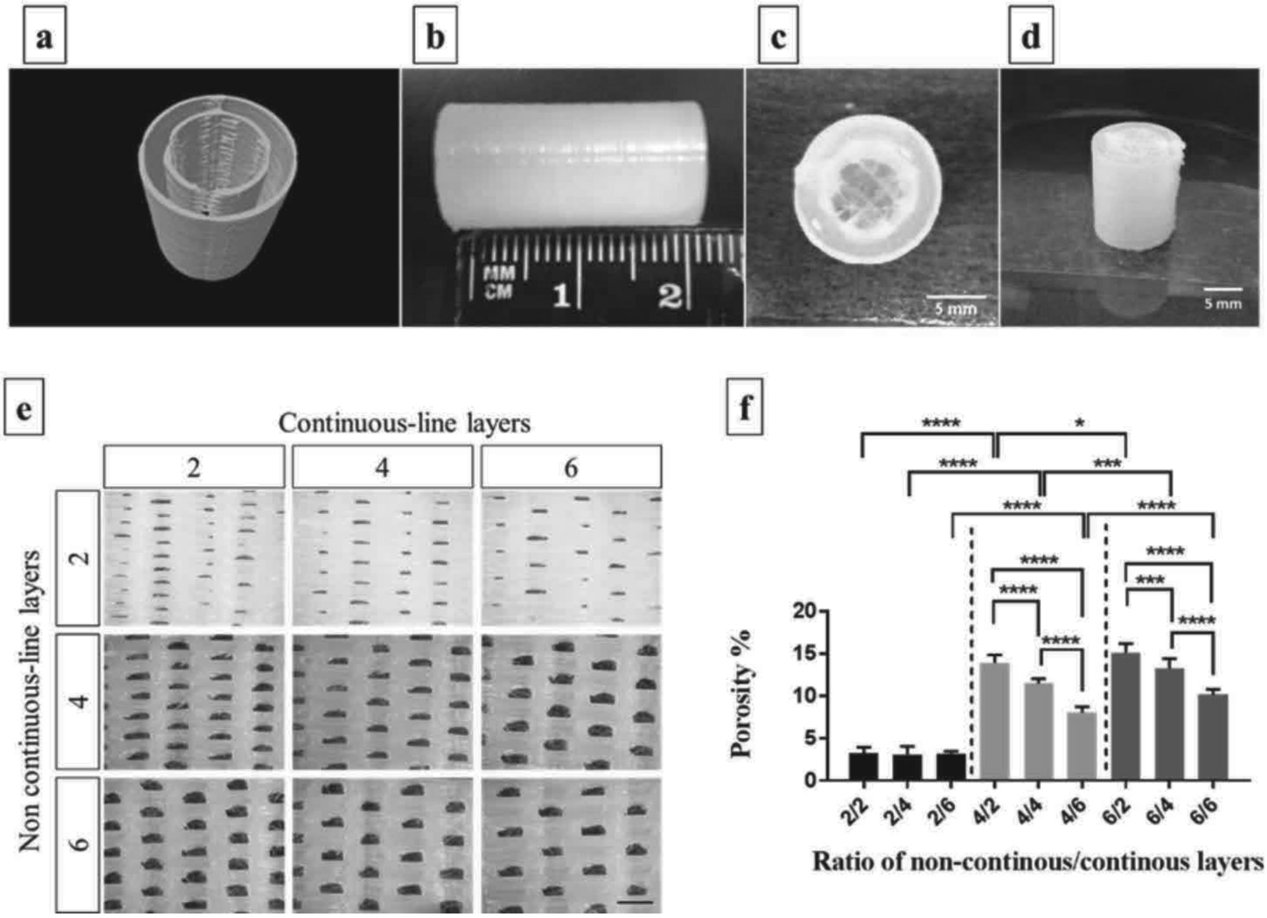

Figure 2 3D Printing of the PCL-alginate scaffold. (**a**) µCT image of the PCL scaffold. (**b-d**) Optical images of the final PCL-Alginate hydrogel scaffold. (**e**) Optical images of nine porosity patterns of the PCL cylinders. *Images were obtained following unrolling the cylinders, scale bar= 2 mm. (**f**) Porosity of the printed cylinders. The porosity was expressed as a percentage of the total pore area to the total area of the field of view. Significance levels were $^{*}P < 0.05$, $^{***}P < 0.001$ and $^{****}P < 0.0001$.

3.2 Spatial and temporal control of protein concentration

Spatial and temporal concentration gradients of soluble growth factors are crucial for neural tissue development and repair [10, 11]. Therefore, development of a 3D printing method for spatially controlling soluble molecules concentrations within the scaffold would be very useful for directing stem cell differentiation towards nerve regeneration. In this part of the study, the capacity of 3D printing to introduce spatial control of protein concentration within the tubular scaffold was explored using a model protein (FITC-BSA) to produce a linear gradient pattern. This was achieved by reducing the number of layers printed using FITC-BSA-loaded alginate as a function of distance (10-steps gradient graded by 10% reduction in the number of layers per step: **Figure 1-b**). Fluorescence microscope images of the longitudinal cross-section of the scaffold were used to qualitatively characterise the gradient pattern **(figure 3- a and b)**. Confocal imaging of the hydrogel section revealed a gradual reduction in green colour in the longitudinal direction from the base to the top of the scaffold, indicating a concentration gradient pattern of FITC-BSA in the hydrogel cylinder (**figure 3-b**). To further confirm the development of the gradient pattern, a concentration profile of the FITC-BSA was determined as a function of distance, and a linear regression model was used to model the linearity of the printed gradient pattern. This analysis revealed a linear reduction of the FITC-BSA concentration as a function of the distance with $r^2 = 0.93$ and a slope of -0.08, which were reasonably close to the original design **(figure 3-b)**. 3D printing of a linear gradient pattern with a 10-step change in the amount of delivered protein suggested precise control over the spatial concentration of protein immediately after printing.

The temporal presentation of the FITC-BSA gradient in the tubular scaffold was examined following the incubation of the patterned scaffold in PBS for 24 and 48 h at 37°C. An exponential phase decay model was used to model the decay in the gradient pattern. When the printed scaffolds were incubated in PBS without further crosslinking of the alginate hydrogel, there were no obvious gradient patterns as indicated by low values of the coefficient of determination of the exponential decay model (r^2), which were 0.29 and 0.39 after 24 h and 48 h, respectively, in comparison to 0.83 at time zero (**figure 3-d**). However, further crosslinking of the partially crosslinked alginate reduced protein diffusion and release from the scaffold and caused a sustainable gradient pattern following the two incubation periods. The coefficient of determination (r^2) of the fully crosslinked alginate-scaffolds at 24 and 28 h time points were 0.71 and 0.79, respectively, in comparison to their respective values in partially crosslinked alginate-scaffolds (**figure 3-e**). These results demonstrated a controlled temporal presentation of the gradient pattern due to the release of protein into the medium, and the process can be further tuned by increasing the crosslinking density of the hydrogel.

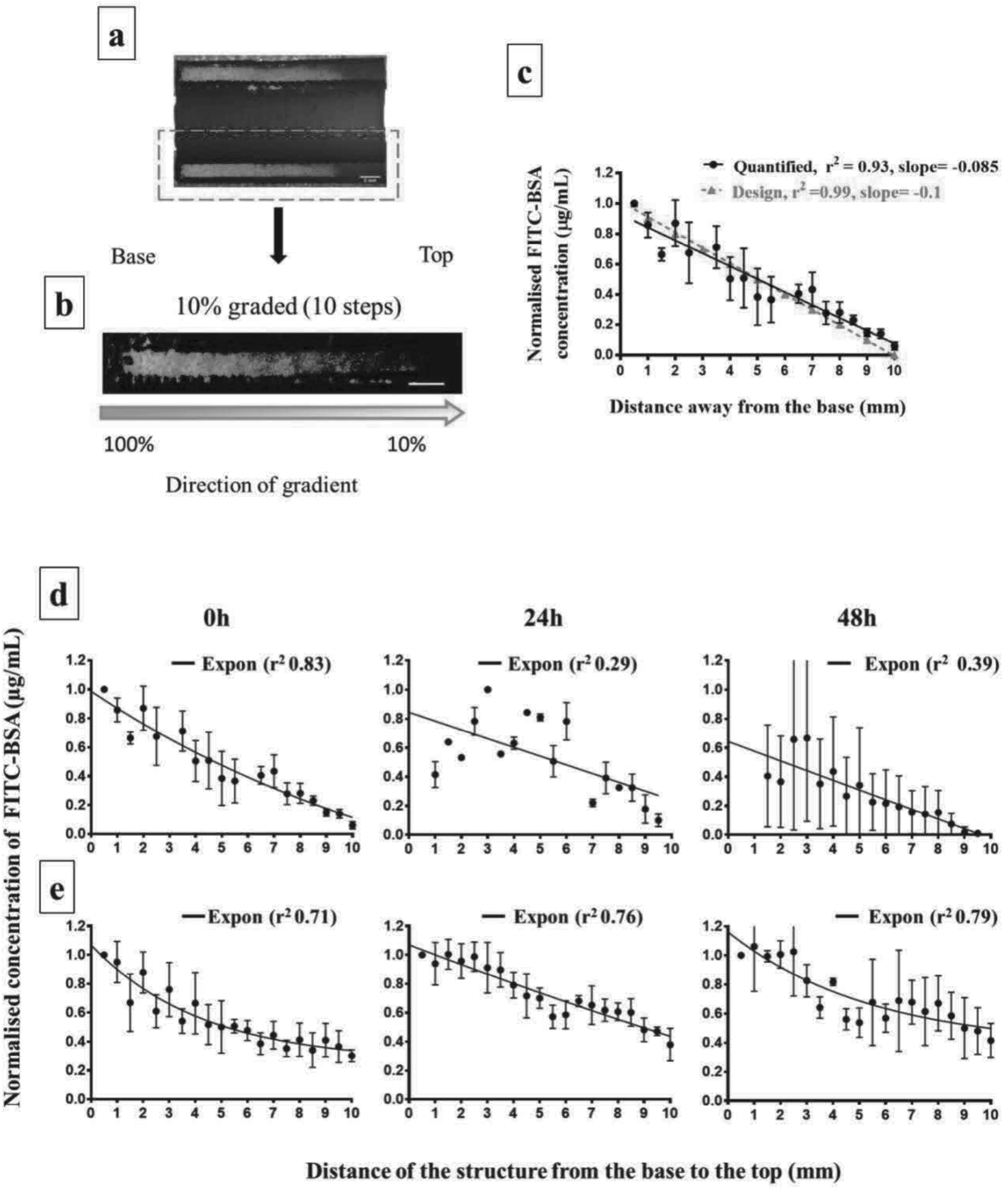

Figure 3 Spatial and temporal control of protein concentration in the scaffold. (**a**) Fluorescence image of the cross-sectioned scaffold showing the hydrogel tube with a FITC-BSA gradient (green colour) , scale bar = 2 mm. (**b**) Confocal image of the cross-sectioned scaffold showing a gradual reduction in the fluorescence intensity (green colour) from the scaffold base; 10-region pattern with a 10% reduction in the FITC-BSA containing layer between the successive regions was printed, scale bar= 2 mm(note: 20 mm long scaffolds were used in **a&b** to demonstrate gradient pattern). (**c**) Quantification of the FITC-BSA concentration gradient showing a linear gradient. (**d**) Temporal concentration gradients of FITC-BSA in 3D printed PCL-Alginate scaffolds in PBS at zero, 24 & 48 h (without crosslinking) or (**e**) with post-printing crosslinking of alginate. An exponential decay model was used to distinguish between gradient and homogenous patterns of the protein in **d&e**. For (**c**), (**d**) and (**e**), each point represents concentration of the FITC-BSA per 0.5 mm thick stack (10 µm slice × 50) and the values were normalised to their respective higher concentration regions values. Values are mean ± SD, N=3-4, R=3. (note: 10 mm long scaffold were used in c, d and e for quantification analysis).

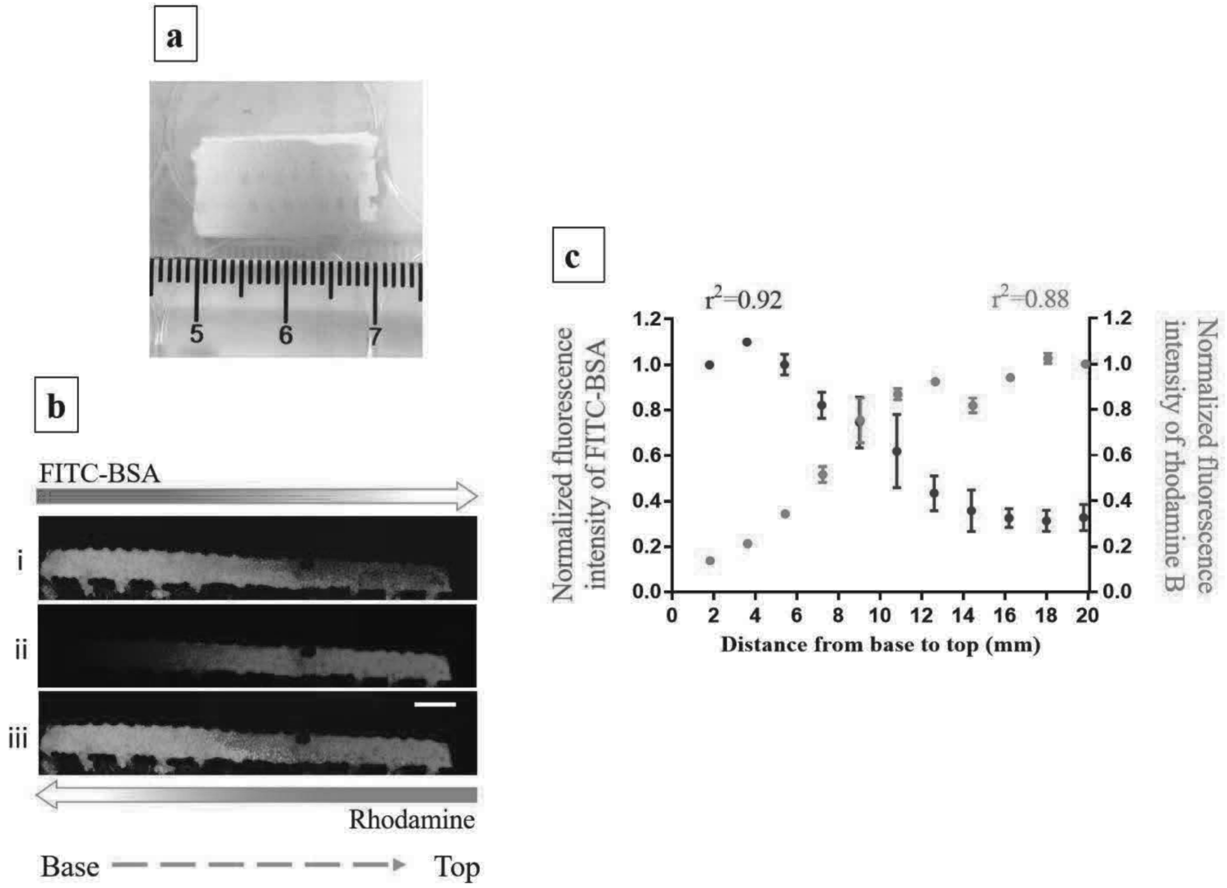

Figure 4 3D printing of PCL-alginate scaffold with opposite gradients. (**a**) Optical image of the scaffold with FITC-BSA (green) and rhodamine (red) (*the outer PCL cylinder was removed). (**b-i**) Confocal images of the cross-sectioned structure showing the FITC-BSA gradient (base to top), and (**b-ii**) the rhodamine gradient (top to base) and (**b-iii**) the overlay, scale bar = 2 mm. (**c**) Quantification of spatially opposite gradients; each point represents the average of fluorescence 100 pixels per 1.8 mm distance of the scaffold retrieved from image analysis of two scaffolds using Image J software (version 1.52e). Fluorescence values were normalised to the fluorescence intensity value at highest region in each gradient pattern

Furthermore, the capacity of the above described method to create tubular scaffolds patterned with two opposite gradients was also explored. Optical and confocal macroscope images of the hydrogel cylinder retrieved from a tubular scaffold printed with two opposite gradient patterns show two opposite and overlapping gradient patterns of FITC-BSA (green) and rhodamine (red) (**figure 4 a and b**). **Figure 4-c** shows the normalised fluorescence intensity of FITC-BSA and rhodamine as a function of the scaffold distance, confirming the capability of accurate creation of opposite overlapping gradient patterns. These results confirmed the capacity of this 3D printing approach to create multiple, overlapped opposite gradient patterns as dictated by the design.

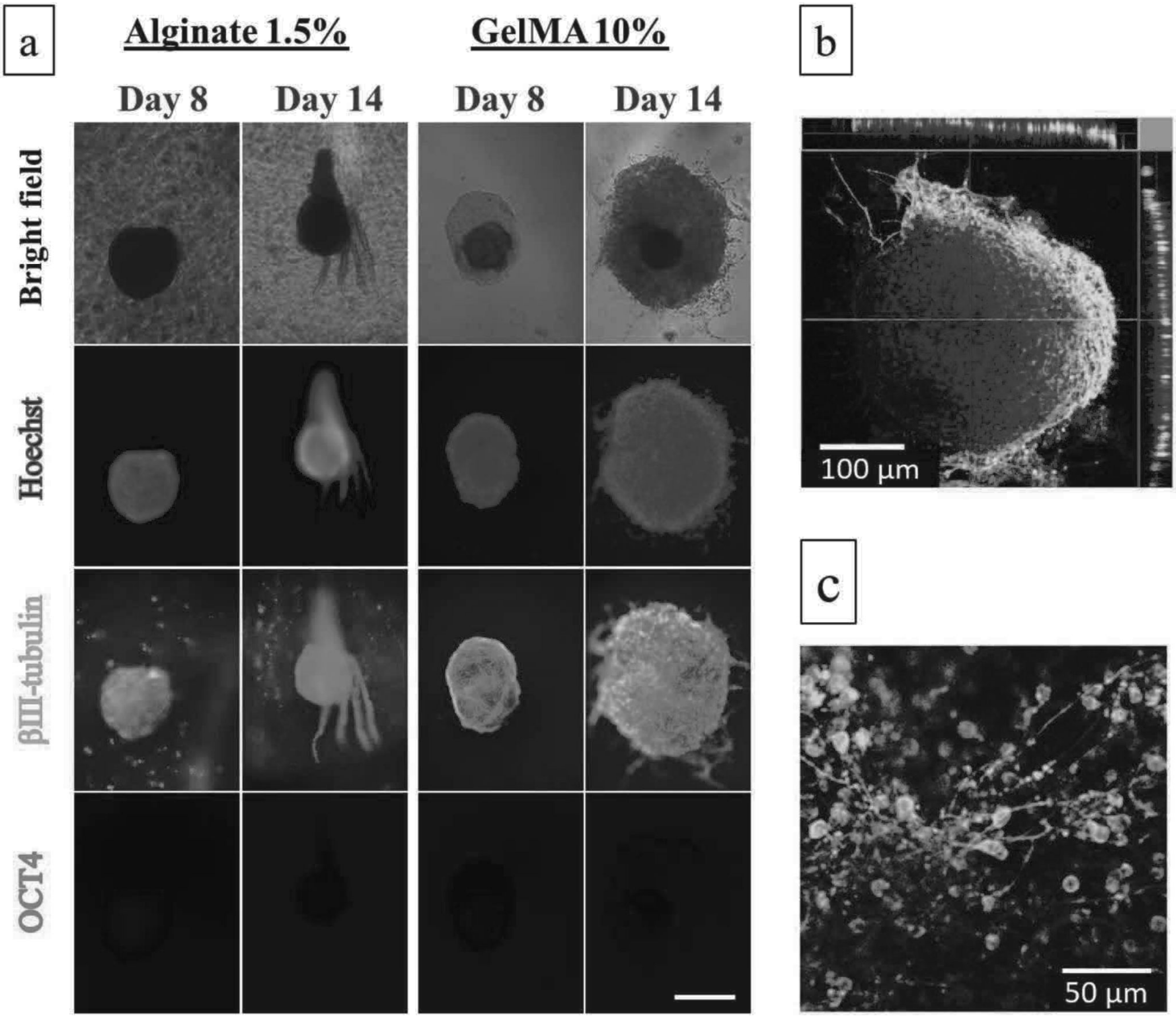

Figure 5 Neural differentiation of EBs in 3D hydrogel. (a)Immunocytochemistry analysis at days 8 and day14 for early neuronal marker β III tubulin (in green) and pluripotency marker OCT4 (in red) of the EB suspended in two different hydrogels, alginate (1.5%) and GelMA (10%). The images are representative of three replicates, Scale bar=200 µm. Confocal laser microscopy images of EBs differentiated in 10% GelMA (day 14) (b) 3D orthogonal view of the Z-stack (c) 2D image at 20X magnification, showing the neuronal morphology and neurites outgrowth.

3.3 3D Bioprinting of EBs in GelMA

In order to print a 3D model that can replicate the developmental neurogenesis, an EBs-laden tubular scaffold was printed and its capacity to induce neural differentiation and patterning was investigated. EBs were chosen because they give rise to the neural progenitor cells that are responsive to morphogens and can differentiate into different neuronal identities. A preliminary experiment to investigate neural differentiation of EBs in hydrogel was performed. Two hydrogels, alginate (1.5%) and GelMA (10%), were initially investigated for EBs encapsulation, growth and neural differentiation. Although EBs differentiated in alginate hydrogel were βIII-tubulin positive (weak signal), there was no clear growth of EBs, spreading of cells around the EBs or neuronal morphology. In contrast, EBs differentiated in GelMA shows strong βIII-tubulin expression with a clear increase in EBs Size and spreading of axonal-like extensions around the EBs zone (**figure 5-a**). Further, laser confocal microscopy images were used to confirm the 3D structure of the EB in GelMA matrix (**figure 5-b**) and neuronal morphology (**figure 5-c**). This result suggests the suitability of GelMA for differentiation of EBs. Thereafter, GelMA hydrogel was selected as a bioink to print an EBs-laden tubular scaffold and 3D bioprinting of EBs-laden GelMA was optimised. Rheological characterisation of the GelMA hydrogel shows a reduction in viscosity in response to an increase in hydrogel temperature, confirming viscosity and thermo-responsive behaviour of GelMA (**figure 6-a)**. However, the viscosity of 2.5% GelMA was much lower than the viscosities of 5% and 10% GelMA, even at very low temperatures (~4ºC), inferring its poor printability, particularly with a wide bore needle suitable for cell bioprinting. The thermo-responsive behaviour of GelMA allowed for the reduction of shear forces and effective mixing of EBs with hydrogel at 37ºC (low viscosity), and effective encapsulation and bioprinting at 18-20 ºC. The shear thinning, viscoelastic behaviour and gelling temperature of different GelMA concentrations were also confirmed using the oscillatory test (**figure S2**, supplementary information). Based on the rheological characterisation, 5% GelMA was chosen for 3D bioprinting of EBs. EBs-laden 5% GelMA was printed using a straight G20 needle (ID 600 µm) and different printing temperatures (5-20 ºC). EBs printed at temperatures 5-17 ºC were dissociated and the cells were damaged, as shown by phase contrast and live/dead staining images (**figure 6-b)**. However, EB integrity and their cell viability were preserved when the printing temperature was increased to 18-20 ºC (**figure 6-b**). These results suggest that a reduction in viscosity, in response to an increase in hydrogel temperature, reduces the shear stress forces and prevents EB dissociation during extrusion. This suggested that a viscosity threshold should not be exceeded to avoid EBs dissociation during extrusion, which was determined to be around 601 Pa.s for GelMA hydrogel (viscosity corresponding to a printing temperature of 18 ºC (**figure 6-a**). 3D printing of 5% GelMA at temperatures above 20 ºC was challenging due to the significant reduction in hydrogel viscosity, resulting in a liquid-like hydrogel which did not support strand formation upon extrusion from the needle.

On top of viscosity, the needle’s internal diameter (ID) and shape are crucial factors that determine the shear stress forces during extrusion, and consequently EB integrity, viability or proliferation[29]. To test the effect of needle diameter and shape, needles with two different shapes (straight and tapered) and two different diameters (G22 and G20) were used to print EB-laden 5% GelMA structures. Results revealed that the highest post-printing proliferation rate was achieved with straight G20 needle **(figure 6-c)**, which resulted in a 3-fold increase in the metabolic activity at day 8 when normalised to metabolic activity at day 2. A two-fold increase in metabolic activity was achieved for EBs printed using tapered G22 and tapered G20, similar to results obtained for non-printed EBs. However, no increase in metabolic activity was seen for the EB printed using tapered G22 needle. These results suggested a combined effect of needle shape and diameter on EB cell proliferation. The results obtained by measuring metabolic activity were also confirmed by those from the Live/Dead assay (**figure S3, supplementary information**).

3D Bioprinting of an EB-laden 5% GelMA lattice structure using straight G20 needle produced a regular lattice structure with reasonable strand diameter (0.8 mm) in relation to the needle diameter (**figure 6-d**). Live/dead staining of the EB-laden lattice further confirmed the results of proliferation assay and showed a homogenous distribution of EBs through the GelMA strand.

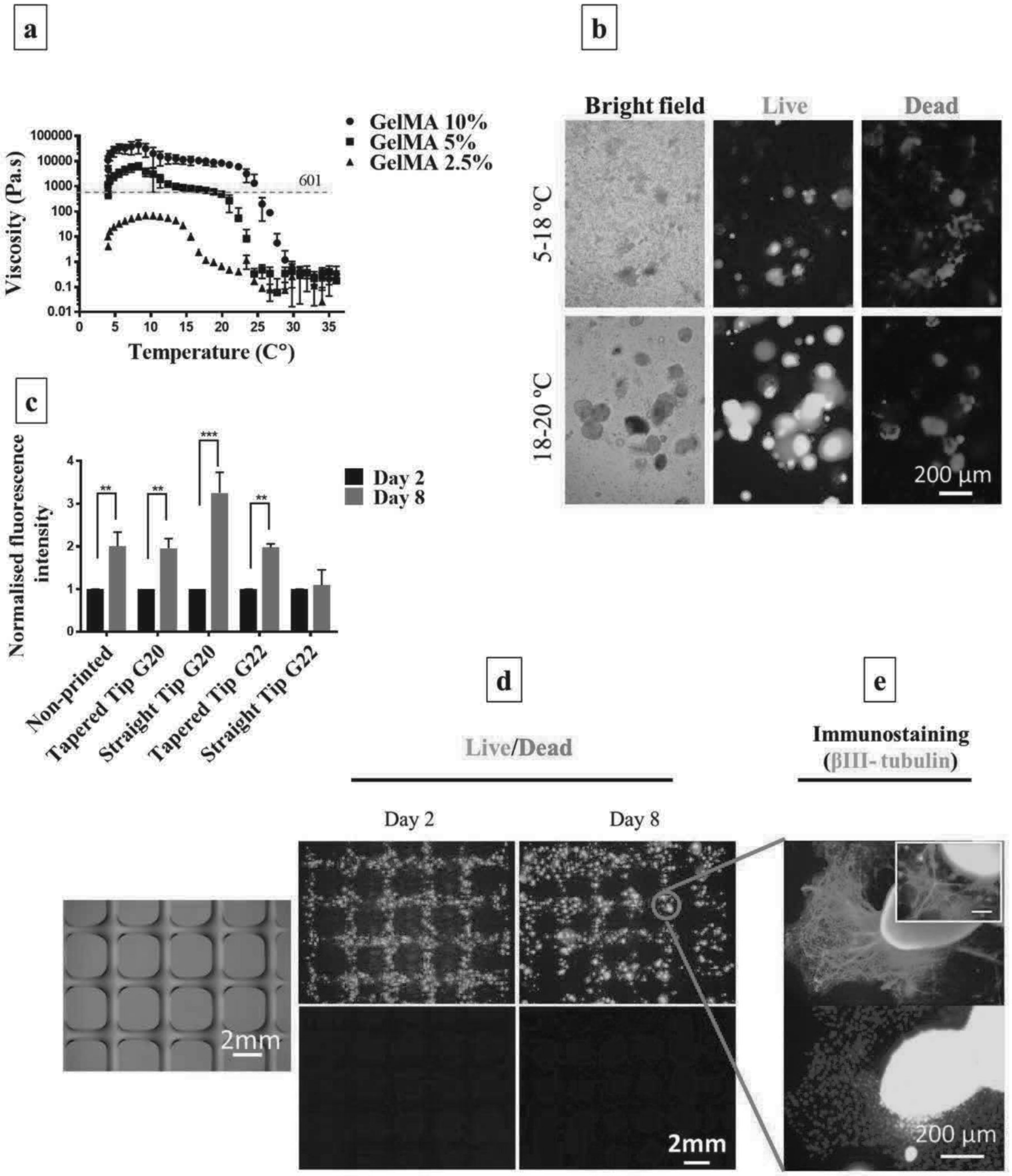

Figure 6 Optimisation of EB-laden bioink (GelMA) for 3D bioprinting. Viscosity of GelMA hydrogels as a function of temperature and concentration. Values are mean ± SD, N=3. (**b**) Post-printing viability of EBs printed within 5% GelMA using a range of printing temperatures (5-20 ºC) using Live/dead stain. (**c**) Post-printing EBs proliferation as a function of time and different needle shape and gauge. Values are mean ± SD, N=3. (**d**) Post-printing cell viability (live/dead assay) as a function of culture time. EBs were printed within 5% GelMA using a straight G20 needle and 5mm/s printing speed at 18°C. (**e**) Post-printing immunostaining of EBs at differentiation day 14. βIII tubulin (green) and Hoechst (blue) stains showed wide spreading of neurons around the EBs zone with neurites extensions (magnification 20X, scale bar = 100 µm).

To characterise post-printing neural differentiation of the EB-laden structures, the printed EB-laden GelMA structures were cultured in N2B27 medium for 12 days and the medium was supplemented with 1µM RA from day 1 to day 3, and then fixed and immunostained for βIII tubulin. Immunocytochemistry analysis shows a large number βIII tubulin positive neuronal cells, and cell spreading around the EBs with a network of neurite extensions, confirming the suitability of the GelMA matrix to support neural differentiation (**figure 6-e**). These results suggested that 3D bioprinting of EB-laden GelMA is feasible and the printed EBs were able to proliferate and differentiate in neurons within the GelMA matrix. However, careful optimisations of hydrogel viscosity and needle diameter were indispensable to minimise the shear stress forces during bioprinting.

3.4 3D Bioprinting of EBs-laden PCL/GelMA scaffold

To biofabricate a hydrogel-based tubular scaffold capable of directing the neural differentiation of ESCs, EB-laden PCL/GelMA scaffold (12 mm × 8 mm × 10 mm) (outer diameter × inner diameter × length) was printed. As a control study, PCL-free EB-laden 5% GelMA rectangular structures (10 mm × 10 mm × 2 mm) (width × length × height) were printed, and cell viability of the printed EB in both structures was evaluated at different time points. At day 8, the images show that EBs printed in the single porous-cylinder PCL/GelMA scaffold were viable (**figure 7, panel-b**). However, the encapsulated EBs showed less spreading around the EBs zone and less EBs cavitation when compared to the EBs encapsulated in the PCL-free rectangular structures (**figure 7, panels a and b**). At day 14, cell viability of some EBs within the single porous cylinder PCL/GelMA scaffolds was reduced as indicated by the presence of the red ethidium bromide colour, suggesting that oxygen and nutrient perfusion through the PCL scaffold may be insufficient. To scrutinise this, a new PCL scaffold with improved porosity was designed and printed. The new scaffold was composed of two macro-porous concentric PCL cylinders (inner and outer) and was called a two porous-cylinders scaffold; thereby the total porosity of the PCL scaffold was doubled. Following the 3D printing of the EB-laden GelMA in the two porous-cylinders scaffold, EBs showed more growth and cell spreading through the hydrogel and cell viability at day 14 was improved when compared to those EBs grown in the one porous-cylinder scaffold (**figure 7, panel c)**.

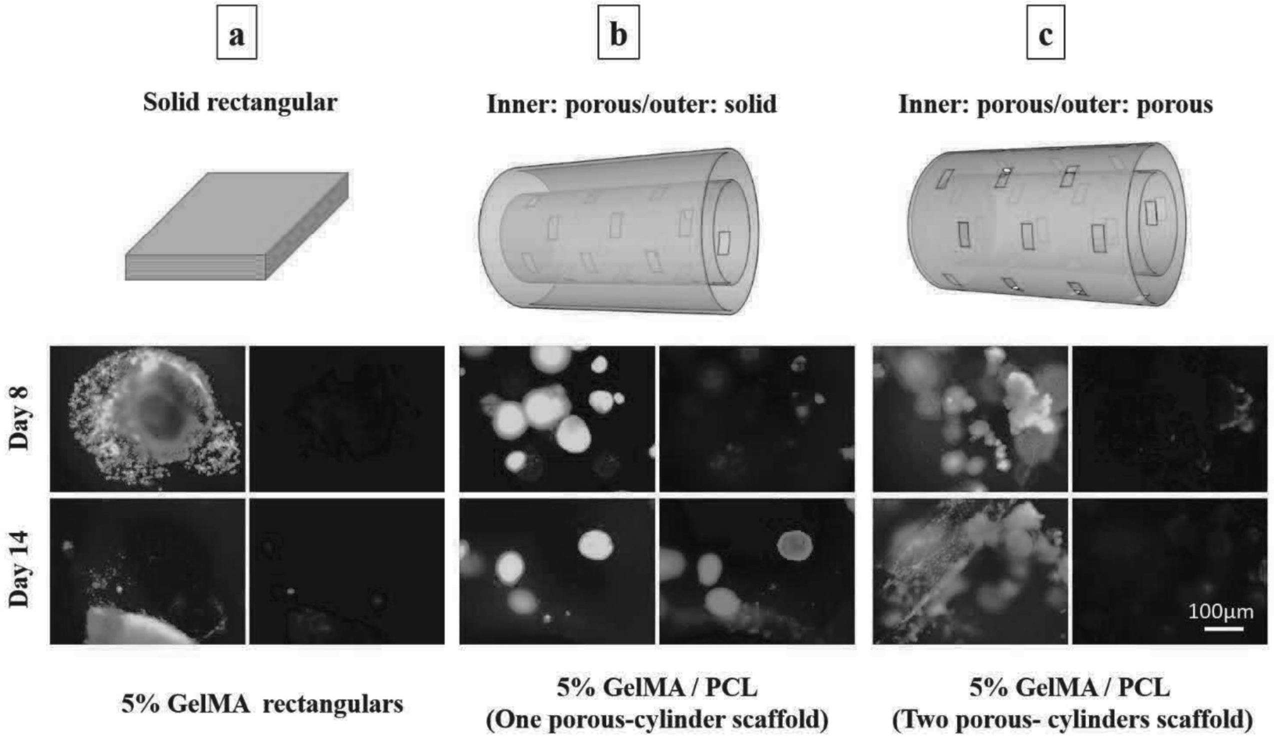

Figure 7 Viability of EBs printed in PCL/GelMA scaffolds. Representative live/dead images, at day 8 and 14, of the EBs printed in **Panel a**: GelMA alone rectangular block, **Panel b**: PCL-alginate with single inner porous PCL cylinder and **Panel c**: PCL-alginate with double porous inner and outer PCL cylinders. (**panel c**). Images are representative of three replicates and 4-5 viewing field were analysed for each scaffold.

3.5 Directed neural differentiation in EBs 3D bioprinted in PCL/GelMA

Figure 8-a shows a schematic diagram of the concept of RA-gradient patterned tubular scaffold and the 3D printed tubular scaffolds (using RA loaded GelMA or RA-free GelMA), representing the higher and the lower ends of the proposed gradient. As a proof of concept that co-bioprinting of EBs and signalling molecules could induce neurogenesis and neuronal patterning, two EB-laden 5% GelMA hydrogels (one loaded with 1µM RA and the other RA-free) were used for bioprinting of the rectangular structures (control study) and PCL/GelMA scaffolds as described previously.

Figure 8-b shows the immunocytochemistry analysis of the neuronal differentiation marker (βIII tubulin), anterior (brain) identity marker (OTX1, 2) and posterior (spinal cord) identity marker (HOXC4) in the EBs differentiated in both RA-free and RA-loaded structures. In the PCL-free rectangular structures, a heterogeneous growth of EBs was observed regardless of the presence of RA. In addition, the EBs showed extensive growth βIII tubulin-positive cells with neurite outgrowth and networking. Regarding neuronal identity pattern, downregulation of the anterior identity (forebrain and midbrain) marker OTX1, 2 and upregulation of the spinal cord marker HOXC4 were observed in response to the presence of 1 µM RA-loaded GelMA. In contrast, EBs differentiated in RA-free GelMA expressed weak but detectable OTX1, 2 signal, and exhibited clear downregulation of HOXC4 (**figure 8, b panel i).** These results suggest that 3D printing of RA as a morphogen can induce neuronal patterning and GelMA hydrogel can retain the printed RA for adequate time to cause neuronal patterning.

EBs within the PCL-GelMA scaffolds exhibited a similar trend of neuronal patterning to that of EBs differentiated within PCL-free GelMA rectangular structures. However, the size of the EBs and cell spreading around them was less in PCL-GelMA scaffolds than that in PCL-free rectangular structures in both RA-loaded and RA-free groups (**figure 8, b panel ii**). These findings proved that 3D printing of RA (1µM) -loaded hydrogel can induce differentiation of the EBs into neurons with posterior or caudal identity while 3D printing of RA-free hydrogel induced differentiation of the EBs into neurons with anterior or brain identity. The capacity of using multi-material 3D printing to induce neural differentiation with two different neuronal identities representing the two ends of RA gradient can pave the way to patterning EBs neural differentiation in response to 3D printed morphogen gradients within the scaffolds.

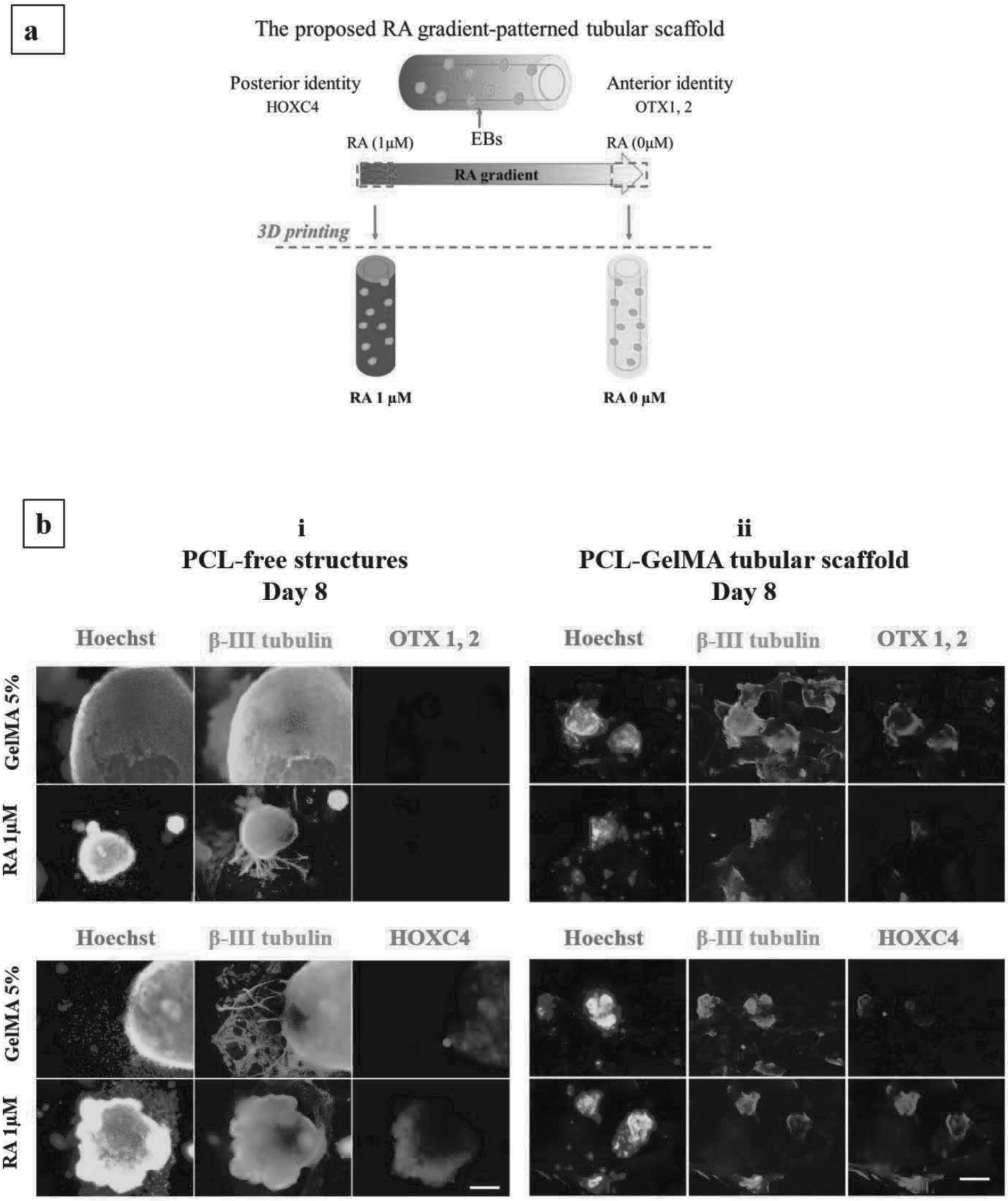

Figure 8 Neural regeneration in 3D printed scaffolds. (**a**) Schematic presentation of the Retinoic acid (RA)-gradient patterned tubular scaffold and the 3D printed tubular scaffolds (using RA loaded GelMA or RA-free GelMA, representing the higher and the lower ends of the proposed gradient as proof of concept). (**b**) Investigation of neuronal positional identity after 3D bioprinting of EBs using RA (1μM)-loaded 5% GelMA hydrogel in **panel i**: GelMA alone rectangular structures and **panel ii** PCL-GelMA scaffolds. Co-immunostaining of the neuronal marker (βIII tubulin) with either anterior positional identity markers (OTX1, 2) or posterior positional identity marker (HOXC4). The images are representative of two replicates and 5-10 EBs were characterized for each replicate. Scale bar = 100 μm.

4 Discussion

This work presents an optimised 3D printing strategy to biofabricate a heterogeneous tubular scaffold that enables directed neural cell differentiation (neural patterning). The scaffold was printed using a multi-material/heads bioprinter which allowed the incorporation of multiple components including PCL, hydrogels, ESC-derived EBs, and signalling molecules in a single composite. The study focused on 3D printing of a tubular scaffold which can serve as a spinal cord conduit or draft, with a concentration gradient of a model fluorescent protein and bioprinting of an EBs within the tubular scaffold. Finally, neural differentiation and patterning of the EBs encapsulated in the tubular scaffold were validated.

Although the presence of a multi-printhead 3D printing machine facilitated biofabrication of complex scaffolds with multiple components, several challenges had to be addressed to create a biomimetic tubular scaffold for nerve regeneration. These included 3D printing of a mechanically stable and supported hydrogel tubular structure, the spatial patterning of signalling molecules, and most importantly 3D bioprinting of viable EBs. Many of these challenges have been reported in previous studies [21, 30, 31].

3D printing of a tubular structure using a soft, printable hydrogel; suitable for neural tissue repair, is a challenging process due to the poor mechanical properties of the hydrogel. This was addressed herein by co-printing with a supporting macro-porous PCL scaffold. PCL has shown good printability (strut width, layer-to-layer attachment and shape fidelity), however, careful optimisation of nozzle and printing environment temperatures were necessary for enhanced shape accuracy and control over porosity. These results were consistent with previous reports using hybrid 3D printing of PCL with hydrogels to reinforce the hydrogels and modulate the scaffold's mechanical properties or porosity [21, 32-34]. The PCL printing method described here allowed for the generation of macro-pores on the surface of the cylinders with precise control over pore size, number and distribution. This enabled the 3D printing of a strong regular structure, together with enhanced nutrients and waste transport for cells or cell aggregates in the hydrogel cylinder.

Concentration gradients of growth factors have been used in nerve regeneration to control neural differentiation of pluripotent stem cells, guide axonal growth and neural cell migration [4, 35, 36]. Recently, 3D printing to spatially control the physical or chemical scaffold properties has raised a particular interest in tissue engineering to create a biomimetic 3D gradient environment [30, 31, 37]. Here, we present a method to spatially control concentrations of soluble molecules within the tubular scaffold using extrusion-based 3D printing. Our results are consistent with previous reports which used 3D printing to spatially control protein concentration [15, 38, 39]. However, most of the previous work was based on inkjet printing of a 2D layer of immobilized protein [39, 40]. As compared to the conventional methods of gradient generation such as microfluidic device [41, 42], or simple diffusion [25], 3D printing of a concentration gradient pattern provides a simple, rapid, accurate and programmable method [38, 40]. The ability of the extrusion-based 3D printing to generate single or dual concentration gradients patterns, which are characterised by linear, opposite, and overlap features, will be very useful to develop more complex 3D biomimetic models capable of controlling ESCs neural differentiation in vitro following the in vivo neurogenesis of development. This ability is of particular importance in biofabrication when combined with other capacities of 3D printing such as cell bioprinting or materials patterning.

EBs are ESC aggregates and routinely used to differentiate ESCs into neurons, as they can give rise to neural progenitor cells [43], which represent neuroectodermal progenitors that exist during embryonic development. These cells can be directed to form neurons with different neuronal positional identities or subtypes if exposed to the appropriate chemical and/or physical cues [44, 45] such as morphogens. In this context, 3D bioprinting of EB-laden hydrogels offers a novel strategy to encapsulate EBs in a functionalised 3D hydrogel matrix, which can further direct them to neurons with a specific positional identity or subtype using selected morphogen concentration gradients [17]. 3D bioprinting of EB-laden hydrogels can allow better control over multiple chemical and physical cues. Several reports have used hydrogel to encapsulate and differentiate EBs [17, 46, 47], however, this is to our knowledge the first report using this 3D printing technology to form an EB-laden hydrogel matrix.

To select the suitable hydrogel for neural differentiation and 3D bioprinting of EBs, EBs were first differentiated in two hydrogels matrices, alginate and GelMA. The neural differentiation permissive properties observed for GelMA in comparison to alginate hydrogel supported the choice of GelMA for encapsulation and printing of EBs. Previous studies have shown that GelMA supports cell adhesion [48] and neural differentiation, including enhancement of axonal growth of mESCs [46, 49]. Also, GelMA rheological properties, such as shear thinning and thermo-responsiveness allowed fine-tuning of shear stress, making it feasible to preserve EBs viability during encapsulation and 3D bioprinting. These results are consistent with a previous report [50]. EB-laden 5% GelMA was successfully extruded using a G20 needle at 18-20 °C, following careful optimisation of hydrogel viscosity and needle diameter to preserve the spherical morphology, viability and proliferation of the EBs. EBs printed in 5% GelMA matrix showed a homogenous distribution in the matrix, and neuronal differentiation was achieved as indicated by neurite outgrowth and positive expression of βIII-tubulin, comparable to that of non-printed EBs differentiated in suspension culture. Several studies have used tissue spheroids (cell aggregates) for bioprinting of tissues, however they were as a biomaterial-free bioink [51-54].

As a proof of concept of the concentration-dependent control of the neural differentiation using the described 3D printing approaches, EBs were printed using 1 μM RA-loaded and RA-free GelMA representing both higher and lower ends of the proposed RA-gradient range. In PCL-GelMA structures, the co-expression of βIII tubulin and HOXC4 markers indicated neural differentiation and caudalisation (posterior identity) of the EBs printed with RA, which was comparable to those printed in the PCL-free GelMA structures. This result is consistent with the *in vivo* [12, 55] and *in vitro* effects of RA [56, 57]. Although RA is a small molecule and not expected to remain in the hydrogel matrix for extended periods, our results indicate that RA was retained post-printing in the GelMA matrix for sufficient time to pattern cells toward a caudal (hindbrain to the spinal cord) identity. This is in line with the findings of other studies that short term (< 24 h) exposure of EBs to RA is sufficient to induce neuronal patterning [45, 56]. More investigations will now be conducted using different morphogens (such as SHH, RA and BMP) in opposite and orthogonal directions to develop spatiotemporally stable gradients able to induce neural cell patterning. Moreover, differentiation of EBs towards the glial cell lineage using morphogen gradients should also be investigated in the future to create a more physiological functional system. Neuronal differentiation of the EBs using 3D bioprinting of a single RA concentration suggests that this method can be further extended to more complex 3D printing of morphogen gradient patterns to direct the neural differentiation of stem cells.

5 Conclusion

In conclusion, multi-head 3D printing strategy was employed to biofabricate a complex biomimetic tubular scaffold. The described 3D printing approach demonstrated 3D printing of a mechanically stable and macroporous tubular scaffold comprised of thermoplastic polymer and hydrogel. This research has developed a method to spatially control morphogen concentration within the tubular scaffold generating spatiotemporal gradient patterns of soluble factors. 3D bioprinting of an EB-laden GelMA hydrogel and an EB-laden tubular scaffold was successfully demonstrated. The EB-laden PCL/GelMA tubular scaffold supported EB differentiation toward a neuronal fate with caudal (or spinal cord) identity in response to co-printing with RA, suggesting the potential of co-printing of hydrogel, cells and signalling molecules to direct neural differentiation into specific neuronal identities. This strategy could be further developed to create a nerve conduit supporting spatially patterned neural differentiation using co-bioprinting of EBs with specific growth factor gradients (such as SHH and BMP). Such in-vitro models offer more insights to tissue engineering for biomimetic neural developmental studies and spinal cord repair.

6 Conflicts of interest

There are no conflicts to declare.

7 Acknowledgements

This work is a part of the PhD project of the first author and the authors would like to acknowledge the financial support of the higher committee for education development in Iraq (HCED), Iraqi Prime Minister Office, Green zone, Baghdad, Iraq. The authors also would like to thank Professor Kevin Shakesheff for is kind support of this project. Omar Hamid thanks Dr Evangelos Delivopoulos and Dr Omar Qutachi for their scientific and technical support of this project.

8 References

[1] R.Y. Tam, T. Fuehrmann, N. Mitrousis, M.S. Shoichet, Neuropsychopharmacology, 39 (2014) 169-188.
[2] Y. Gao, Z. Yang, X. Li, Regenerative Biomaterials, 3 (2016) 115-122.
[3] J.W. Fawcett, Trends in Neurosciences, 41 (2018) 239-242.
[4] A. Tedeschi, F. Bradke, Current Opinion in Neurobiology, 42 (2017) 118-127.
[5] A. Raspa, R. Pugliese, M. Maleki, F. Gelain, Biotechnology and bioengineering, 113 (2016) 253-259.
[6] M. Tsintou, K. Dalamagkas, N. Makris, Neural Regeneration Research, 15 (2020) 425-437.
[7] K.S. Straley, C.W. Foo, S.C. Heilshorn, Journal of neurotrauma, 27 (2010) 1-19.
[8] Y.S. Chen, H.J. Harn, T.W. Chiou, Cell transplantation, 27 (2018) 407-422.
[9] K. Dalamagkas, M. Tsintou, A. Seifalian, A.M. Seifalian, International journal of molecular sciences, 19 (2018).
[10] H.L. Ashe, J. Briscoe, Development, 133 (2006) 385-394.
[11] M. Cohen, J. Briscoe, R. Blassberg, Current Opinion in Genetics & Development, 23 (2013) 423-428.
[12] M. Maden, Nature reviews. Neuroscience, 8 (2007) 755-765.
[13] X. Cao, M.S. Shoichet, Neuroscience, 103 (2001) 831-840.
[14] D. Mortimer, Z. Pujic, T. Vaughan, A.W. Thompson, J. Feldner, I. Vetter, G.J. Goodhill, Proceedings of the National Academy of Sciences, 107 (2010) 5202-5207.
[15] J.B. N., L.K. Z., Z. Gehua, H. Junyun, G.M. K., K.Y. Lin, E.E. A., K.K. D., J. Alex, M. Fanben, E.L. W., J. Xiaofeng, M.M. C., Advanced Functional Materials, 25 (2015) 6205-6217.
[16] J. Jang, J.Y. Park, G. Gao, D.W. Cho, Biomaterials, 156 (2018) 88-106.
[17] H. Qi, Y. Du, L. Wang, H. Kaji, H. Bae, A. Khademhosseini, Advanced materials (Deerfield Beach, Fla.), 22 (2010) 5276-5281.
[18] S. Suri, A. Singh, A.H. Nguyen, A.M. Bratt-Leal, T.C. McDevitt, H. Lu, Lab on a chip, 13 (2013) 4617-4624.
[19] P. Zhuang, A.X. Sun, J. An, C.K. Chua, S.Y. Chew, Biomaterials, 154 (2018) 113-133.
[20] S.F. Collins, Stem cells and development, 23 Suppl 1 (2014) 79-82.
[21] S.V. Murphy, A. Atala, Nat Biotech, 32 (2014) 773-785.
[22] D. Liu, H. Zhang, F. Fontana, J.T. Hirvonen, H.A. Santos, Advanced drug delivery reviews, 128 (2018) 54-83.
[23] C.B. Highley, C.B. Rodell, J.A. Burdick, Advanced materials (Deerfield Beach, Fla.), 27 (2015) 5075-5079.
[24] J. Malda, J. Visser, F.P. Melchels, T. Jungst, W.E. Hennink, W.J. Dhert, J. Groll, D.W. Hutmacher, Advanced materials (Deerfield Beach, Fla.), 25 (2013) 5011-5028.
[25] H.M. Eltaher, J. Yang, K.M. Shakesheff, J.E. Dixon, Acta Biomaterialia, 41 (2016) 181-192.
[26] H. Wichterle, M. Peljto, Current protocols in stem cell biology, Chapter 1 (2008) Unit 1H.1.1-1H.1.9.
[27] R.Z. Lin, Y.C. Chen, R. Moreno-Luna, A. Khademhosseini, J.M. Melero-Martin, Biomaterials, 34 (2013) 6785-6796.
[28] L. Ruiz-Cantu, A. Gleadall, C. Faris, J. Segal, K. Shakesheff, J. Yang, Materials Science and Engineering: C, 109 (2020) 110578.
[29] A. Blaeser, D.F. Duarte Campos, U. Puster, W. Richtering, M.M. Stevens, H. Fischer, Advanced healthcare materials, 5 (2016) 326-333.
[30] S.M. Bittner, J.L. Guo, A.G. Mikos, Bioprinting, 12 (2018) e00032.
[31] L.G. Bracaglia, B.T. Smith, E. Watson, N. Arumugasaamy, A.G. Mikos, J.P. Fisher, Acta Biomaterialia, 56 (2017) 3-13.
[32] Y. Yu, Y. Zhang, I.T. Ozbolat, Journal of Manufacturing Science and Engineering, 136 (2014) 061013-061013.
[33] Y. Shanjani, C.C. Pan, L. Elomaa, Y. Yang, Biofabrication, 7 (2015) 045008.
[34] L. Ruiz-Cantu, A. Gleadall, C. Faris, J. Segal, K. Shakesheff, J. Yang, Biofabrication, 8 (2016) 015016.
[35] R.J. McMurtrey, Journal of tissue engineering, 7 (2016) 2041731416671926-2041731416671926.
[36] N. Bhattacharjee, A. Folch, Microsystems &Amp; Nanoengineering, 3 (2017) 17003.
[37] C. Li, L. Ouyang, I.J. Pence, A.C. Moore, Y. Lin, C.W. Winter, J.P.K. Armstrong, M.M. Stevens, Advanced Materials, 31 (2019) 1900291.
[38] E.D. Miller, J.A. Phillippi, G.W. Fisher, P.G. Campbell, L.M. Walker, L.E. Weiss, Combinatorial chemistry & high throughput screening, 12 (2009) 604-618.
[39] S. Ilkhanizadeh, A.I. Teixeira, O. Hermanson, Biomaterials, 28 (2007) 3936-3943.
[40] P.G. Campbell, E.D. Miller, G.W. Fisher, L.M. Walker, L.E. Weiss, Biomaterials, 26 (2005) 6762-6770.
[41] O.C. Amadi, M.L. Steinhauser, Y. Nishi, S. Chung, R.D. Kamm, A.P. McMahon, R.T. Lee, Biomedical microdevices, 12 (2010) 1027-1041.
[42] E. Weibull, S. Matsui, M. Sakai, H. Andersson Svahn, T. Ohashi, Biomicrofluidics, 7 (2013) 064115.
[43] Y. Maury, J. Côme, R.A. Piskorowski, N. Salah-Mohellibi, V. Chevaleyre, M. Peschanski, C. Martinat, S. Nedelec, Nature biotechnology, 33 (2014) 89.
[44] Y. Okada, T. Shimazaki, G. Sobue, H. Okano, Developmental biology, 275 (2004) 124-142.

[45] A. Ranga, M. Girgin, A. Meinhardt, D. Eberle, M. Caiazzo, E.M. Tanaka, M.P. Lutolf, Proceedings of the National Academy of Sciences of the United States of America, 113 (2016) E6831-e6839.

[46] C.R. Kothapalli, R.D. Kamm, Biomaterials, 34 (2013) 5995-6007.

[47] S. Battista, D. Guarnieri, C. Borselli, S. Zeppetelli, A. Borzacchiello, L. Mayol, D. Gerbasio, D.R. Keene, L. Ambrosio, P.A. Netti, Biomaterials, 26 (2005) 6194-6207.

[48] J.W. Nichol, S.T. Koshy, H. Bae, C.M. Hwang, S. Yamanlar, A. Khademhosseini, Biomaterials, 31 (2010) 5536-5544.

[49] B. Jun Hyuk, L. Jong Min, C. Bong Geun, Biomedical Materials, 11 (2016) 015019.

[50] T. Billiet, E. Gevaert, T. De Schryver, M. Cornelissen, P. Dubruel, Biomaterials, 35 (2014) 49-62.

[51] J.M. Kelm, V. Lorber, J.G. Snedeker, D. Schmidt, A. Broggini-Tenzer, M. Weisstanner, B. Odermatt, A. Mol, G. Zünd, S.P. Hoerstrup, Journal of Biotechnology, 148 (2010) 46-55.

[52] V. Mironov, R.P. Visconti, V. Kasyanov, G. Forgacs, C.J. Drake, R.R. Markwald, Biomaterials, 30 (2009) 2164-2174.

[53] C. Norotte, F.S. Marga, L.E. Niklason, G. Forgacs, Biomaterials, 30 (2009) 5910-5917.

[54] M.A. Skylar-Scott, S.G.M. Uzel, L.L. Nam, J.H. Ahrens, R.L. Truby, S. Damaraju, J.A. Lewis, Science Advances, 5 (2019) eaaw2459.

[55] R. Lara-Ramirez, E. Zieger, M. Schubert, The international journal of biochemistry & cell biology, 45 (2013) 1302-1313.

[56] A. Meinhardt, D. Eberle, A. Tazaki, A. Ranga, M. Niesche, M. Wilsch-Brauninger, A. Stec, G. Schackert, M. Lutolf, E.M. Tanaka, Stem cell reports, 3 (2014) 987-999.

[57] E.O. Mazzoni, S. Mahony, M. Peljto, T. Patel, S.R. Thornton, S. McCuine, C. Reeder, L.A. Boyer, R.A. Young, D.K. Gifford, H. Wichterle, Nature neuroscience, 16 (2013) 1191-1198.